Smoothing and Cicatrization of Isotactic Polypropylene/Fe 3 O 4 Nanocomposites via Magnetic Hyperthermia

Pablo Griffiths, Simon Fritz, Laura Ea, Florent Dalmas, Jérôme Adrien, Vivien Truchot, Françoise Méchin, Cyril Benoit, Fabien Dutertre, Jean-Charles Majesté, et al.

Smoothing & Cicatrization of iPP/Fe_3O_4 Nanocomposites via Magnetic Hyperthermia

Pablo Griffiths,[†] Simon Fritz,[†] Laura Ea,[†] Florent Dalmas,[†] Jérôme Adrien,[†] Vivien Truchot,[‡] Françoise Méchin,[‡] Cyril Benoit,[¶] Fabien Dutertre,[¶] Jean-Charles Majesté,[¶] Niels Pernoux,[§] Jerome Grando,[‖] Jerome Chevalier,[†] and Guilhem P. Baeza[*,†]

[†]*INSA Lyon, Universite Claude Bernard Lyon 1, CNRS, MATEIS, UMR5510, 69621, Villeurbanne, France*

[‡]*INSA Lyon, Universite Claude Bernard Lyon 1, Universite Jean Monnet, CNRS, UMR 5223, Ingénierie des Matériaux Polymères, F-69621, Villeurbanne, France*

[¶]*Université de Lyon, CNRS, Université Claude Bernard Lyon 1, INSA Lyon, Université Jean Monnet, UMR 5223, Ingénierie des Matériaux Polymères F-42023, Saint-Etienne Cédex, France*

[§]*Lines Manufacturing, 67810, Holtzheim, France*

[‖]*Plastic Omnium Intelligent Exterior System, 01150, Sainte-Julie, France*

E-mail: guilhem.baeza@insa-lyon.fr

Abstract

We prepare industrially relevant magneto-responsive thermoplastic nanocomposites capable of being cicatrized and smoothed after additive manufacturing through the application of an oscillatory magnetic field (OMF). The materials are made of an isotactic polypropylene (iPP) matrix filled with magnetite nanoparticles (2-22 wt.%, 75 nm in diameter) synthesized from steel waste, providing them with a limited ecological impact on top of their ability to be repaired. Nanoparticles are found to have no significant impact on the thermal properties of the iPP, which allows to compare directly the magneto-thermal effect measured on the different nanocomposites. Beyond the primary temperature increase generated by magnetic hysteresis loss, we evidence that the OMF irradiation triggers a second heating mechanism from the iPP melting. This phenomenon, which was assigned to nanoparticles magnetization and subsequent rotation causing high-frequency mechanical friction, is here investigated in a systematic way. Our results indicate that while the specific power generated by nanoparticles friction is (expectedly) proportional to the irradiation time, it is independent of the nanoparticles content as long as the temperature is well-above the polymer melting point. These observations suggest therefore that the (local) filler-polymer interfacial rheology dictates the amount of heat generated through friction. From an application point of view, 7 wt.% of nanoparticles is found to be enough to induce iPP melting from magneto-thermal effect, which enables the post-processing of hot-pressed and 3D-printed specimen through "cicatrization" and "smoothing" experiments. In the former case, rewelding samples cut into two pieces is found to provide similar Young modulus and yield point as in native hot-pressed samples (exhibiting however a lower strain at failure). In the latter case and beyond the improved specimen appearance, smoothing is found to double both the stress and strain at failure of large 3D-printed samples that present nevertheless significantly lower properties than their hot-pressed counterparts.

Keywords: magnetic hyperthermia, magnetothermal effect, nanocomposites, healing, polypropylene, magnetite, 3D-printing

Introduction

Beyond every types of *recycling* including chemical and mechanical approaches, increasing the lifespan of common plastic and rubber-based materials is one of the greatest challenges to achieve a more sustainable development. In this context, spreading *reusing* and/or *repairing* philosophies is crucial and has attracted the attention of many research groups in the two last decades. A well-known example (from 2008) is that of self-healing soft matter where the control of inter-molecular bonds provides "supramolecular" networks with the astonishing ability to auto-repair at room temperature without external stimulus.[1] Another emblematic example from the same group relies on inorganic (silica) particles serving as stitches to cicatrize gels and biological tissues.[2] Since then, a wide range of supramolecular networks based on small molecules have emerged, including vitrimers, covalent adaptable networks, and dissociative networks,[3] offering vast possibilities in terms of mechanical/rheological properties. In addition, polymer-based supramolecular networks known as "sticky-" or "associative-" polymers have also been extensively studied for their rich rheological behavior,[4,5] opening promising perspectives both in terms of processing and self-repairability.[6–8]

It seems nevertheless that these major advances in chemistry did not materialize yet into daily applications where self-healing materials remain sparsely used. While this lack of societal impact certainly resides in the cost/complexity of the materials involved, other issues regard their stability *vs.* thermo-oxidation[9] and humidity.[10] In addition, the required molecular mobility ensuring self-healing is most often antagonistic to high mechanical performances, particularly at high deformation, which drastically limits the fields of application. An interesting example is that of Bouteiller et al. who have tentatively addressed these limitations by modifying chemically a commercial (relatively strong and tough) thermoplastic polyurethane in order to enable its self-healing without major loss of mechanical properties.[11]

Apart from increasing the complexity of chemical architectures, materials healing can be envisaged through the application of various physical stimuli including but not limited to convective heat, microwaves,[12,13] laser radiations[14,15] and magnetic oscillatory fields.[16–20]

In the latter case, stimulus-healing is achieved by irradiating micro- or nanoparticles (NPs) embedded into a thermoplastic polymer matrix with an oscillatory magnetic field (OMF) of several hundreds of kHz and 5-50 mT, generating heat through magnetic hysteresis loss. The physical mechanism at the origin of this loss depends on the particles' size, shape and nature.[21] It consists of Néel (and possibly Brown) relaxation(s)[22,23] into single magnetic domain particles whereas it is dominated by walls motion into multi-domain ones.[24] On the other hand, eddy currents only appear in the case of macroscopic electric conductors (> 1 mm). The advantages of magnetic hyperthermia *vs.* other healing methods reside in the combination of the following facts: i) the treatment can be performed in a contactless manner, including without visual path, ii) the heat can be controlled by tuning both the OMF characteristics and the sample formulation, iii) the absence of susceptor ensures low thermal inertia and minimize energy consumption and iv) the temperature field can be modified based on the NPs localization.

While magnetic mechanisms are activated as soon as the OMF is turned ON and keep on producing heat as long as it is not turned OFF, mechanical friction between NPs and the polymer matrix has been identified as an extra-heating mechanism. It was first suspected in hydrogels,[25] semi-crystalline homopolymers[26] and supramolecular networks,[27] and recently clarified through X-ray scattering techniques in thermoplastic polyurethanes (TPU).[28] In every cases, the sudden drop of viscosity (*e.g.* melting) following the temperature rise primarily caused by magnetic hysteresis loss triggers the particles motion, enabling them to rotate at the frequency of the OMF. In addition, their progressive polarization may also lead to translation resulting into the formation of dipolar chains.[17,28] Overall, melting-triggered friction modifies the time evolution of the material's temperature, denoted $T(t)$ hereafter, from a simple "Box-Lucas" exponential rise profile[29] to a "double-bump" one.[17] The combination of both magnetic and mechanical effects on $T(t)$ has been recently theorized by Helbig et al.[30] in the case of superparamagnetic, isolated and spherical NPs dispersed into a Newtonian fluid, which in spite of the advanced physical description, represents a canonical (*i.e.*, simple)

example of responsive material. Extending this model to nanocomposites made of a rheologically complex matrix like a homopolymer melt filled with possibly non-spherical[31,32] and aggregated NPs[33] represents a great challenge for the coming years. Quantitative predictions of $T(t)$ curves is actually expected to strongly contribute to the fundamental understanding of NPs rotationnal diffusion in complex soft matter.

In this work, we focus on the peculiar case of isotactic polypropylene (iPP) that is massively used in the transport industry for its low cost, high mechanical properties and lightness to design car bumpers and body elements.[34,35] Conversely to our previous work dealing with a relatively short TPU matrix (weight averaged molar mass $\overline{M_w} = 120$ kg mol^{-1} and molar mass dispersity, Đ= 2) characterized by a low zero-shear viscosity of about $\eta_0 = 100$ Pa s,[17] the typical average molecular weight used for iPP based engineering goods is $\overline{M_w} = 200 - 300$ kg mol^{-1} and Đ ≈ 4, resulting in a melt viscosity of a few kPa s right above the melting point. From an application point of view, this difference is crucial since an efficient cicatrization can only be performed on the condition that the polymer mobility is high enough, corresponding to a rapid macroscopic flow. We demonstrate below that iPP healing is indeed achievable, opening the way to further industrial development.

The article is organized as follows: the materials and the wide range of experimental techniques used to characterized the composites are described in section II. The results obtained on the neat iPP matrix and four composites containing a growing content of NPs are presented and discussed in section III. Thermal investigations by DSC, magnetic hyperthermia curves ($T(t)$) and rheological dynamic frequency sweeps first allow to characterize i) the ability of the material to generate heat under the OMF and ii) flow rapidly enough above the melting point. Based on these fundamental results, we then focus on the most industrially relevant formulation on which we perform both cicatrization and smoothing procedure. The former consists of re-welding specimens cut into two pieces while the latter aims to reduce the surface roughness of 3D-printed parts. The performance of these two "healing" methods are evaluated through uniaxial tensile tests and scanning electronic microscopy.

Materials and Methods

Materials

Polymer matrix

The polymer matrix is a commercial isotactic polypropylene (iPP) graciously provided by Total (France). Its weight average molar mass is $\overline{M_w} = 199\,\mathrm{kg\,mol^{-1}}$ and its molar mass dispersity is$Đ = 4.5$. The corresponding steric exclusion chromatography elution curve is provided in Supporting Information (SI) **Section 1**.

Magnetic fillers

"PGL" (commercial name) magnetite nanoparticles (Fe_3O_4) were purchased from Hymagin' (France). They mainly consist of elementary particles of $d_{50} = 75$ nm forming unbreakable aggregates of a few hundreds of nm in diameter. The main interest of this powder resides in its synthesis route involving steel waste as a raw material. The patented technology[36] is entirely based on reactions with water and does not require any volatile organic solvent, strong acid nor flammable gases, fitting well the sustainable developement philosophy developped in the present work.[37] The powder's X-ray diffraction pattern, a thermogravimetric analysis and a Fourier transfrom infra-red spectrum are provided in **SI Section 1**. The two latter analyses suggest the presence of small amount of organic species at the powder surface in spite of the organics-free synthesis route, possibly improving the powder dispersion in the iPP matrix.

Nanocomposites compounding (small scale)

iPP/Fe_3O_4 nanocomposites were prepared by twin-screw extrusion in a $15\,\mathrm{cm^3}$ chamber (DSM Xplore, The Netherlands). Appropriate amount of polymer and magnetic fillers were handed-mixed and poured into the extruder so that the nominal mass fraction of magnetite within the nanocomposites was 2, 7, 16 and 22 wt.%, corresponding to ca. 0.3, 1.3, 3.1 and 4.5 vol.%. The extruder chamber was pre-heated at 210 °C ensuring the quick melting of the

polymer. The rotor speed was set to 40 rpm and the mixing time to 6 min. The so-prepared nanocomposites were then hot-pressed at 210 °C for 3 min and slowly cooled down in air. The film thickness was fixed to 1 mm, serving to prepare samples for magnetic hyperthermia characterization as well as rheological and tensile tests.

Nanocomposites compounding (large scale) and additive manufacturing

For large-scale 3D-printing (see below), larger quantities of nanocomposites were prepared using a corotating twin-screw extruder EUROLAB 16 (Thermofisher, United-Kingdom). The screw diameter and the length/diameter ratio were $D = 16$ mm and $L/D = 40$, respectively. The device was divided into 10 sectors starting from the *feeding* zones to the 4 mm diameter *exit die*. The barrel temperature was fixed to 210 °C, with a gradual increase from room temperature to 150 °C between the *feeding* zones and zone 2. iPP pellets and Fe_3O_4 NPs were simultaneously introduced at feeding rates of 880 g h^{-1} and 120 g h^{-1} ($x_{NP} \approx 7$ wt.%) using two twin-screw gravimetric feeders (Brabender and Coperion K-Tron). A specific screw profile, consisting of various forwarding screw elements (*feeding* and *conveying* zones) and two successive *mixing* zones was designed to optimize the mixing procedure. Details on the twin-screw configuration are reported in **SI Section 2**. After cooling at room temperature, the extruded strand was finally pelletized to feed the 3D-printer.

Pellets were processed through the additive manufacturing system Lines SONIC, (Lines Manufacturing, France), capable of producing parts up to 2500 mm in all $\vec{X}, \vec{Y}, \vec{Z}$ directions. This three-axis gantry high-speed additive manufacturing production machine was equipped with a Fused Granular Fabrication (FGF) technology consisting of a raw material processing unit coupled with a screw extrusion setup and a melted material deposition device that enables high speed printing up to a theoretical value of 2000 mm s^{-1}. The actual deposition speed for iPP based nanocomposites was however set to 800 mm s^{-1}. Similarly as for the compounding step, the screw temperature was fixed to 210 °C. Once melted, the material entered the deposition unit where the temperature (210 °C), flow rate (125 cm^3 min^{-1}) and

flow pressure (16 bars) were carefully monitored and regulated before coming out of the 3.5 mm diameter nozzle. .

Methods

Differential Scanning Calorimetry (DSC)

Experiments were run on a DSC-8000 (PerkinElmer, USA) under a nitrogen flow of 20 mL min^{-1} at 5 °C min^{-1}. Samples were first cooled down to 20 °C and heated up to 250 °C ($50 - 200$ °C displayed). This cycle was then repeated once, resulting in the measurements displayed in Figure 1. Additional thermograms for different thermal history including 3D-printed samples are available in **SI Section 3**.

X-ray Diffraction (XRD)

X-ray diffraction measurements were performed at room temperature on a D8 advance apparatus (Bruker, USA) using Cu Kα_1 radiation. The diffraction pattern of the PGL Fe_3O_4 powder was recorded in the 2θ range of $20 - 90$ °.

Scanning Electron Microscopy (SEM) and Focused Ion Beam (FIB)

For large magnification microstructural observations (Figure 6), sectioning and imaging of the nanocomposites were investigated using a dual column focused ion beam (FIB)-scanning electron microscope (SEM) ZEISS NVision40. A Ga^{2+} ion beam accelerated at 30 kV was used. A two-step milling procedure was employed on bulk nanocomposites that were metalized with gold beforehand. First, a bulk trapezoid was milled at high current beam (13 nA) so that the shorter face could be imaged by the electron beam up to a minimum depth of 25 μm. Then, a final polishing of the observed surface was carried out with a fine current beam (150 pA). SEM images of the polished surface were then recorded with an accelerating voltage of 5 kV, using an in-lens secondary electron (SE) detector. Such imaging conditions

allow observation of insulating materials with minimal charging effects, high resolution, and a good contrast between the inorganic and organic phases.[38]

Low magnification micrographs of the 3D-printed specimens (Figure 8) were obtained using a VEGA3 scanning electron microscope (TESCAN, USA), operating at a 15 kV acceleration voltage with a secondary electron detector. Transverse cross-sections of fractured tensile test specimens were analysed with or without magnetic induction smoothing. Additionally, longitudinal sections were observed on a cryocut sample after undergoing smoothing treatment.

X-ray tomography

X-ray tomography was carried out at room temperature on a V-TomeX device (GE Phoenix X-ray GmbH, USA) with a 2520 V detector from Varian. We used 80 kV and 280 μA as X-ray parameters, placing the sample vertically with a voxel size of 3 μm. Nine hundreds radiographs with an exposure time of 333 ms and 3 radiographs averaged at each step were recorded during the 360° rotation of the sample for a total acquisition time of 20 min.

Rheology

Dynamic frequency sweep measurements were performed with a strain-controlled rheometer (ARES, 2KFRTN1 from Rheometric Scientific, currently TA, USA) using stainless steel parallel plates of 8 mm diameter. The samples thickness was set to *ca.* 1.0 mm. The temperature was fixed to 210 °C. The angular frequency was varied from $\omega = 10^2$ to 10^{-1} rad s^{-1}. The strain amplitude was fixed to $\gamma = 3$ % for both iPP and M7 samples.

Tensile Tests

Uniaxial tensile tests were conducted on dog-bone shaped specimen at room temperature with a constant displacement rate of 2 mm min^{-1} using a 1/ME (MTS, USA) apparatus equipped with a 5 kN load cell. Hot-pressed specimens were punched out from thin films with

working dimensions 26.0 × 4.0 × 1.0 mm^3 . Similarly, 3D-printed specimen were punched out from thick sheets resulting in dimensions of 26.0 × 4.0 × 3.4 mm^3 . A minimum of three tensile tests was conducted for each type of sample. The variability of the results is displayed through shaded rectangles in Figures 5 and 7.

Induction heating and thermal imaging

Induction heating was performed with a master controller v3+ apparatus (CEIA, Italy) connected to a two-turns water-refrigerated flat spiral inductor. A 0.1 mm thick Teflon-based composite tape covered the inductor to protect it from material flowing. The frequency of the magnetic field was 855 kHz and its maximum amplitude in the sample was estimated to 10 mT through Comsol simulations.[17] The magnetic field was generated by a current of 19 A in the coil and delivered through pulses of duration t_{pulse} every t_{period}. The apparent power of the inductor was varied from t_{pulse}/t_{period} ranging from 17 to 100 %. Disk-shaped samples (6 mm diameter - 1 mm thick) were submitted to the magnetic field and their temperature was recorded with a PI 640i infrared camera (Optris, Germany) equipped with a 15 × 11° lens characterized by an optical resolution of 640 × 480 pixels and a measurement rate of 32 Hz. Temperatures reported in this work systematically refer to the maximal temperature recorded by the camera (at the center of the sample). Data were processed with the software *Optris PIX Connect* in the $20 - 250$ °C range. We used the default camera calibration from Optris and checked that the temperature well agreed with the value provided by a thermocouple ($\pm 2\%$).[39] Cicatrization of hot-pressed dumbbell specimens consisted of cutting samples into two identical pieces and placing them in a silicone mold of corresponding dimensions equipped with an anti-adhesive bottom part. After a minute of induction heating the healed specimens were extracted from the mold and tested (tensile test or SEM). Smoothing of 3D-printed specimens consisted of a 10 min superficial induction heating performed over the whole operational length and on both sides of the samples.

Results and Discussion

Magnetothermal properties

DSC thermograms of the neat iPP and corresponding nanocomposites are reported in Figure 1, demonstrating that 2-22 wt.% (1-5 vol.%) of Fe_3O_4 NPs do not affect significantly the crystallization of the polymer, for which the melting temperature T_m and the crystalline ratio X_c vary erratically within $161 - 164$ °C and $45 - 50$ % intervals, respectively. (X_c estimations are based on a specific enthalpy of neat crystalline iPP of $\Delta H^* = 168$ J g^{-1}, see ref.[40]). Nevertheless, while the melting peak is rather bimodal at low NPs content, the higher temperature side of the peak seems to disappear progressively with increasing the fraction of NPs, suggesting a slightly hindered spherulites growth. Overall, the weak dependence of the thermograms upon varying the filler content is expected because of the limited amount of fillers and the polar surface of the Fe_3O_4 NPs embedded into a quite apolar iPP matrix.

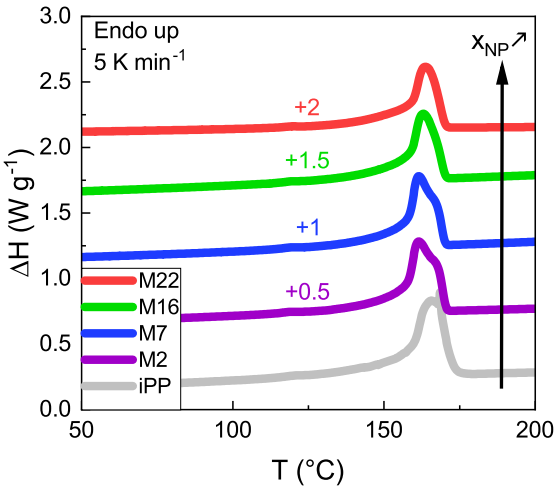

Figure 1: Second heating ramp differential scanning calorimetry thermograms (endo up). Impact of the weight fraction of NPs. Nanocomposites data were vertically shifted for clarity, the shift value (between 0 and 2 Wg^{-1}) is indicated for each sample. The heating rate was fixed to 5 °C min^{-1}. Raw thermograms were normalized by the mass of iPP contained in the samples.

The almost unchanged thermal behavior of the matrix (heat capacity and melting point) makes it possible to compare directly the evolution of the $T(t)$ curves obtained through magnetic hyperthermia, *i.e.*, when the sample is submitted to an oscillatory magnetic field starting from room temperature. The corresponding results are displayed in Figures 2a-d emphasizing the impact of the pulse duration and the NPs content (2d-inset). As expected, increasing the ratio t_{pulse}/t_{period} or the weight fraction of NPs leads to a faster rise of the temperature that possibly reaches the melting point of the matrix (grey zone). In this case, an extra heating mode originating from NPs friction in the viscous polymer systematically emerges,[28] which makes deviate the $T(t)$ curves from a simple exponential rise (or "Box-Lucas" profile) corresponding to the solution of the 0^{th} dimension heat equation for a constant energy flux.[29] All the $T(t)$ curves can be satisfyingly fitted by using the following set of equations

$$\begin{aligned} T(t < t_m) &= T_0 + \Delta T_1 \left[1 - \exp(-(t/\tau_1)^{\beta})\right] \\ T(t > t_m) &= T_0 + \Delta T_1 \left[1 - \exp(-(t/\tau_1)^{\beta})\right] + \Delta T_2 \left[1 - \exp(-(t - t_m)/\tau_2)\right] \end{aligned} \tag{1}$$

where t_m is the time required to activate the second heating mode, *i.e.*, to soften enough the iPP to trigger NPs motion, T_0 is the room temperature, ΔT_1 and ΔT_2 are the temperature amplitudes related to magnetic losses and friction respectively, τ_1 and τ_2 are the corresponding characteristic times, and β (always comprised within the $0.85-1$ interval) is an exponent enabling to slightly "stretch" the first exponential term providing somewhat an error bar on the $T(t)$ profile. All the fit parameters are gathered into Table 1. Here, it is worth to note that the second heating mode systematically emerges from ca. 140 °C, *i.e.*, 10 °C below the onset of the melting peak measured in DSC (Figure 1), which suggests that NPs rotation does not require the matrix to be completely molten. In fact, NPs motion below the melting point could arise from crystalline re-ordering and metastable phases denoted as "rotator phases" or "mesophases" as observed in canonical n-alkanes $6-8$ °C below T_m [41–43] as well as in iPP and similar polymers.[44,45] In addition, the second mode is particularly well-visible

in comparison to our previous work focusing on TPU-based nanocomposites,[17] most likely because of the relatively narrower melting peak and the higher degree of crystallinity of the iPP matrix that implies a gigantic and sudden drop of viscosity at the melting point. By applying the two versions of Equation 1 (with $\beta = 1$), one can then extract the specific power [also called *specific absorption rate* (SAR) in W g^{-1}] associated to each heating mode that can be estimated through

$$SAR_i = \frac{c_{p-i}}{x_{NP}} \frac{\Delta T_i}{\tau_i} \tag{2}$$

where c_{p-i} is the specific heat capacity of the nanocomposites that is measured by DSC at 25 °C and 180 °C, corresponding to the solid- and liquid-states of iPP respectively relevant to quantify the two heating mechanisms. At 25 °C, c_{p-1} = 1.85, 1.84, 1.76, 1.76 and 1.65 J g^{-1} K^{-1} while at 180 °C, c_{p-2} = 3.24, 3.12, 3.12, 3.24 and 3.05 J g^{-1} K^{-1}, respectively for iPP, M2, M7, M16 and M22 specimens. The former values are in fair agreement with the room temperature specific heat capacity tabulated for neat iPP (c_p^{PP} = 1.62 J g^{-1} K^{-1})[46] and magnetite ($c_p^{Fe_3O_4}$ = 0.65 J g^{-1} K^{-1})[47] as well as with the "composites values" provided by a simple mixing rule. Besides, $\frac{\Delta T_i}{\tau_i} = \frac{dT}{dt}|_{t=0}$, the latter term being generally used to evaluate SARs graphically without any data fitting. Note that although ΔT_i and τ_i do not systematically show monotonic trends with x_{NP} and t_{pulse}/t_{period} in Table 1 because of their relative freedom in achieving a good fit on a restricted temperature range, the corresponding SAR_i that quantify the two physical mechanisms do evolve in a consistent way with the pulse duration and the NPs content (Figure 3).

As one may have anticipated, Figure 3a indicates that SAR_1 is systematically proportional to t_{pulse}/t_{period} and does not vary significantly with the NP content. The proportionality was expected since the magnetic losses are cumulated based on the number of magnetization *vs.* incident field ($M = f(H)$) hysteresis loops achieved by the system, itself being directly proportional to the duration of the pulse, *i.e.*, to the t_{pulse}/t_{period} ratio. On the other hand, the constancy of SAR_1 as a function of x_{NP} (Figure 3c) indicates that the

cyclic magnetization of the NPs is not impacted by their dipolar interactions, which seems reasonable given the low NP volume fraction ($\Phi_{NP} < 5$ vol.%). From a quantitative point of view, the quite high values of SAR_1 reaching up to ca. 1000 W g^{-1} are undoubtedly related to the multi-domain ferrimagnetic nature of the nanoparticles and the high frequency of the OMF.

At first sight, it appears that the same logic can be applied to SAR_2 in Figure 3b. In this case, the specific power generated by friction is seen to be proportional to the pulse duration suggesting that the NPs continuously rotate within the polymer matrix as long as the magnetic field is ON, and stop otherwise. In addition, SAR_2 is also observed to be independent of the NPs content above $x_{NP} = 7$ wt.% (*i.e.*, in M7, M16 and M22), which indicates that NPs are not interfering mechanically with each other for experiments shorter than two minutes. Conversely, when non-being 0 (absence of melting), SAR_2 values are much lower in M2, being typically five times less than in the other nanocomposites. This observation can alternatively be made in Figure 3d, where SAR_2 values increase very much between $x_{NP} = 2$ and 7 wt.% before stabilizing. In spite of the lack of direct experimental evidence, we assign this strong deviation to the fact that, for $t_{pulse}/t_{period} = 83$ and 100 %, the steady state temperature in M2 mainly belongs to the polymer melting zone measured from DSC (see Figure 2a), *i.e.*, that the iPP matrix is not completely molten in the experimental time window, limiting therefore the rotational diffusion of NPs.

Interestingly, although SAR_1 is systematically ca. twice as higher than SAR_2, the fact that the two parameters are within the same order of magnitude indicates that the friction mechanism is highly relevant to control the temperature of polymeric fluid submitted to high-frequency magnetic hyperthermia. Said differently, SAR_2 represents here ca. 1/3 of the whole heat generated by the material submitted to the OMF. (Note however that SAR_2 values are hardly predictable since they depend on the amplitude of the multi-domain NPs deflection angle and the rotational friction coefficient that are not directly accessible experimentally in non-Newtonian fluids).[28,30]

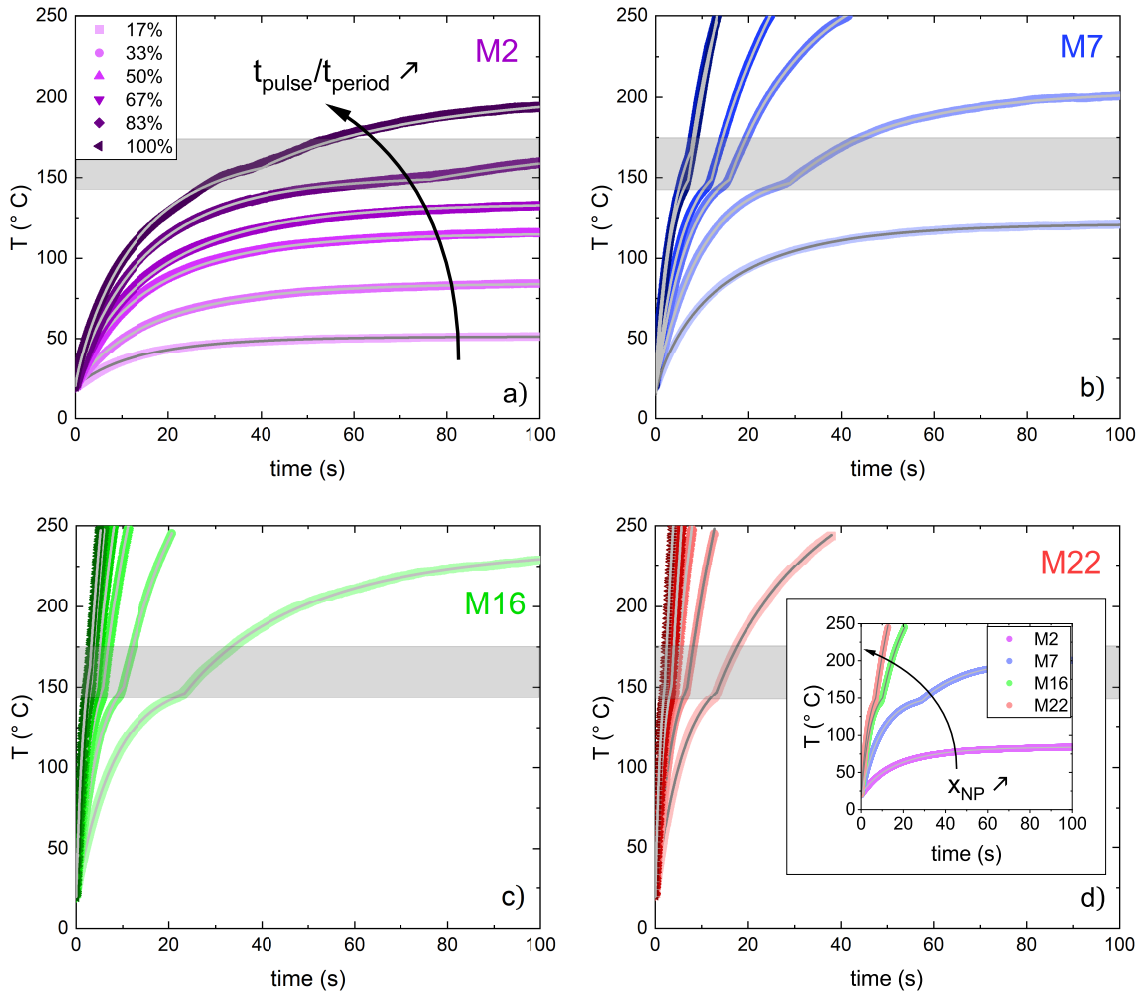

Figure 2: Temperature *vs.* time during induction heating for different values of t_{pulse}/t_{period} in a) M2, b) M7, c) M16 and d) M22 nanocomposites. Inset: Impact of x_{NP} for $t_{pulse}/t_{period} = 33\%$. Grey solid lines are fit to the data with Eq.1. Grey zones represent the temperature range corresponding to the melting peak measured in DSC.

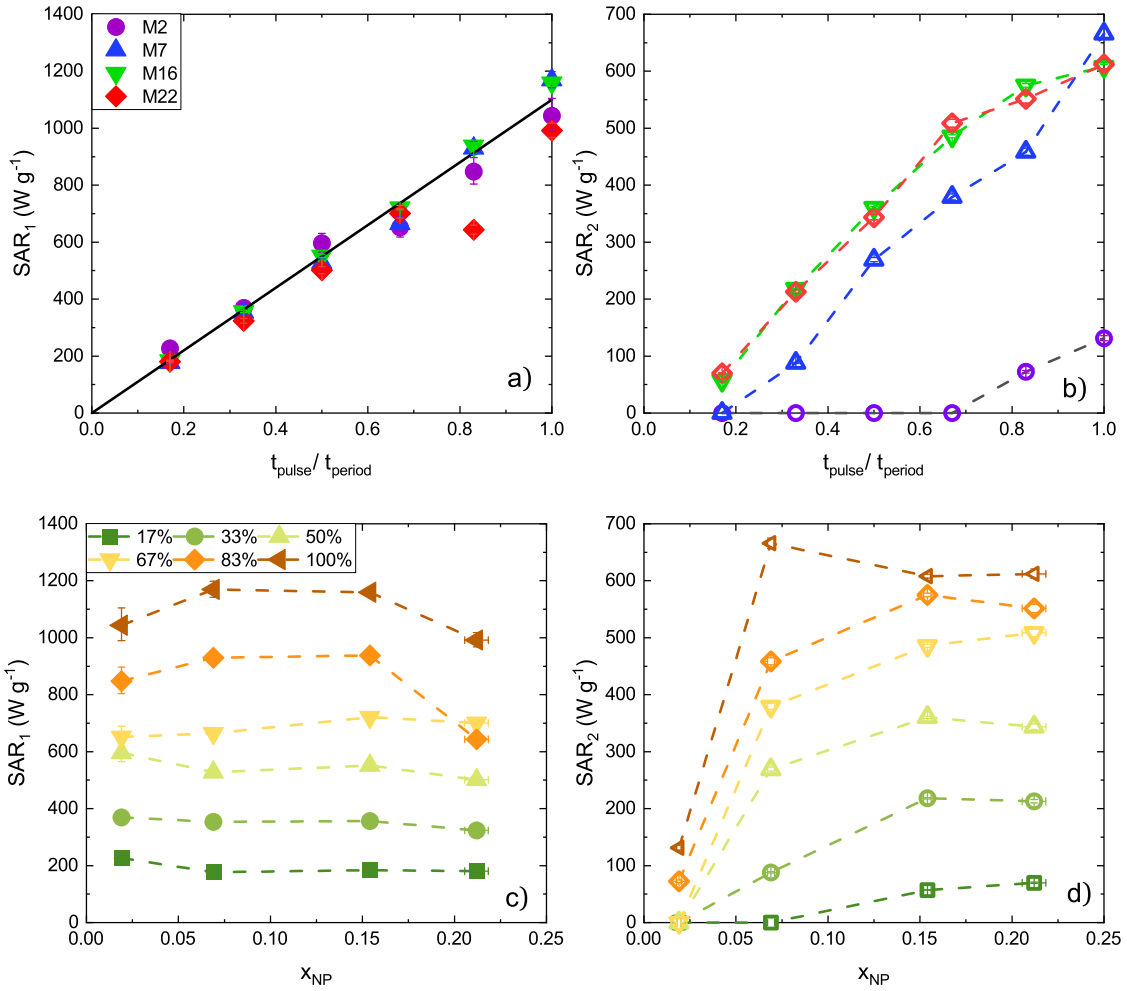

Figure 3: SAR values corresponding to magnetic hysteresis losses (SAR_1) and NPs friction (SAR_2) for various t_{pulse}/t_{period} ratios (a-b) and various content in NPs (c-d). The black solid line in (a) is a fit with an affine function. Note that NPs friction is not detected in M2 for $t_{pulse}/t_{period} < 83\%$, *i.e.*, T_m is not reached, resulting in $SAR_2 = 0$ in (b). Error bars are estimated from thermogravimetric measurements only, their higher and lower limits corresponds to the average value of x_{NP} plus or minus the standard deviation, respectively.

Table 1: Samples characteristics and fit parameters obtained from applying Eq. 1 on $T(t)$ data presented in Figure 2. T_0 (not reported here) is a free parameter varying erratically between 18.4 and 20.5 °C. x_{NP} is measured by thermogravimetric analysis and averaged on three samples. Φ_{NP} is deduced from x_{NP} assuming iPP and Fe_3O_4 densities of 0.9 and 5.1 g cm^{-3}, respectively. Star symbols (*) point data fits providing "surprising" and meaningless individual ΔT_i and τ_i values because of the limited observable temperature range ($T < 250$ °C) related to the IR camera restrictions and iPP degradation. Their ratio $\Delta T_i/\tau_i$, being proportional to SAR_i (see Eq. 2) is however a relevant physical parameter to study, varying in a consistent way with x_{NP} and t_{pulse}/t_{period} (see Figure 3).

Sample –	x_{NP} *wt.%*	Φ_{NP} *vol.%*	X_c %	t_{pulse}/t_{period} -	ΔT_1 ^oC	ΔT_2 ^oC	τ_1 s	τ_2 s	t_m s	β –
iPP	0.0	0.0	50	–	–	–	–	–	–	–
M2	1.9	0.3	46	17	33.2	–	14.2	–	–	0.88
				33	65.2	–	17.2	–	–	0.88
				50	96.8	–	15.8	–	–	0.85
				67	115.2	–	17.2	–	–	0.85
				83	132.4	25.9	15.2	58.7	76.4	0.89
				100	147.0	37.7	13.7	47.2	40.0	0.88
M7	6.9	1.3	46	17	102.4	–	14.8	–	–	0.86
				33	135.7	49.3	9.8	25.3	29.4	0.98
				50	144.6	122.0	7.0	20.5	16.0	1.0
				67	145.5	244.1	5.6	29.1	12.0	1.0
				83	203.7*	146.1*	5.6*	14.4*	7.8	0.8
				100	146.4*	1054.2*	3.2*	71.6*	7.1	1.0
M16	15.4	3.1	45	17	134.3	81	8.3	29.8	23.4	0.99
				33	147.2	169.0	4.7	16.3	10.2	1.0
				50	155.1	309.7	3.2	18.1	5.8	1.0
				67	158.5	337.0	2.5	14.6	4.3	1.0
				83	164.9	984.5*	2.0	36.0*	3.3	1.0
				100	173.2	1156.9*	1.7	40.0*	3.0	1.0
M22	21.2	4.5	46	17	143.3	140.5	6.2	28.9	13.2	1.0
				33	153.3	491.6	3.7	33.2	6.9	1.0
				50	160.4	372.7	2.5	15.6	4.4	1.0
				67	161.5	367.5	1.8	10.4	3.1	1.0
				83	156.5	2000*	1.9	52.2*	3.5	1.0
				100	165.1	2000*	1.3	47*	2.1	1.0

Rheological behavior

Table 1 allows to identify the M7 sample as the most promising material for industrial applications since it appears that 1.3 vol.% of NPs is enough to trigger the iPP melting (almost) regardless of the "inductor power" ($\sim t_{pulse}/t_{period}$). In other words, M7 has *a priori* the ability to be cicatrized and smoothed while being the formulation requiring the least amount of NPs, making it therefore the cheapest to produce and the most likely to flow rapidly. The latter property is actually investigated by performing rheological dynamic frequency sweeps on both the neat iPP and M7. Results are presented in Figure 4 where the storage (G') and loss (G'') dynamic moduli *vs.* the angular frequency measured at 210 °C are reported. As one may have anticipated, adding 1.3 vol.% of NPs is seen to have no significant effect on the rheological behavior of iPP, ensuring therefore M7 to flow at the same rate as the neat homopolymer, corresponding to a zero-shear viscosity $\eta_0 \approx 800$ Pa s. The sample aspect is on the other hand drastically different, passing literally from white to black upon the addition of (only) 1.3 vol.% of Fe_3O_4 NPs (inset of Figure 4), which possibly limits the applications of these materials when used as visible parts.

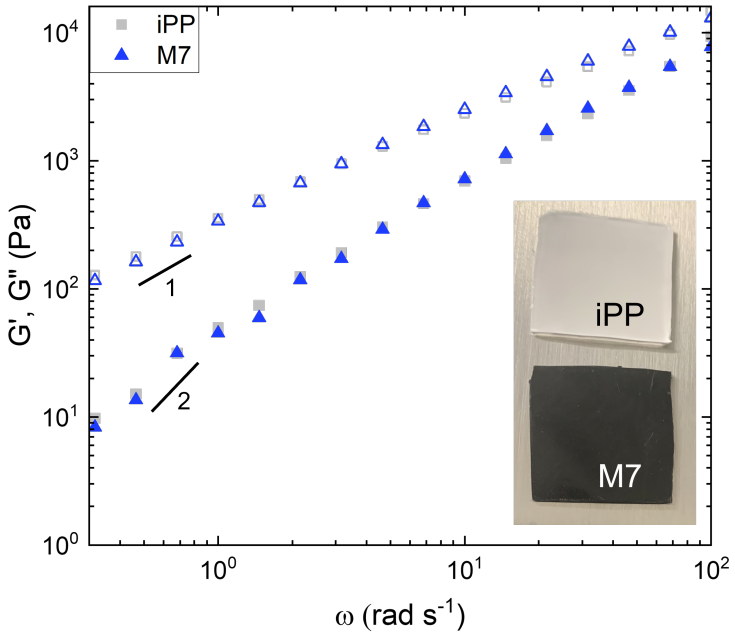

Figure 4: Storage (G', solid symbols) and loss (G'',open symbols) dynamic shear moduli *vs.* angular frequency for neat iPP (squares) and M7 (triangles) samples measured at 210 °C. The canonical G' and G'' slopes corresponding to a Maxwellian fluid are displayed for comparison. Inset: photograph of the neat iPP and the M7 sample emphasizing the drastic change in color with only 1.3 vol.% in Fe_3O_4 NPs.

Cicatrization of hot-pressed specimen

Based on the nanocomposites ability to i) heat above the melting point and ii) flow rapidly, we chose the M7 formulation to produce hot-pressed dumbbell specimens with the aim to test mechanical properties before and after a cicatrization procedure. The latter consisted of cutting a specimen into two pieces with a razor blade and rewelding the material confined into a silicon mold by using localized magnetic hyperthermia similarly as in ref.[17] Tensile tests performed on series of "hot-pressed" samples and their "healed" counterparts are presented in Figure 5. On one hand, "hot-pressed" samples exhibit a Young modulus close to 1 GPa, a yield stress of 18 MPa and an average strain at failure of about 5%. On the other hand, although "healed" samples present similar characteristics in the linear regime, which confirms that a complete cicatrization of the material has been achieved, their failure occur right from the yield point (2-3%), suggesting that in spite of the absence of porosity (see X-ray tomography slides in Figure 6), the iPP chains did not have enough time to fully relax and recrystallize as in the bulk material. In fact, the failure systematically happens in the healed zone whereas it was randomly located in the "hot-pressed" samples - see inset Figure 5 where 1-5 and 6-10 specimen refer to "hot-pressed" and "healed" samples, respectively. At first sight, improving the strain at failure could therefore consist of increasing the healing time or decreasing the viscosity of the polymer. We expect that optimizing these parameters can certainly help but may not be sufficient to recover the original properties. In fact, we demonstrated that by using a similar procedure, responsive thermoplastic polyurethanes of ca. 10 times lower viscosity than the present iPP, also exhibited a significant decrease of their strain at failure after 1 min of cicatrization, passing from ca. 180% down to 120-150% according to the type of NPs.[17] The choice of the filler and their ability to diffuse within the matrix actually represents another pathway to explore.[16,28]

The microstructure of a "hot-pressed" and a "healed" specimen investigated through X-ray tomography and FIB-SEM are presented in Figure 6. As mentioned above, low magnification X-ray tomography slices taken in the $(\vec{X}, \vec{Y})$ plane presented in Figures 6a-b first

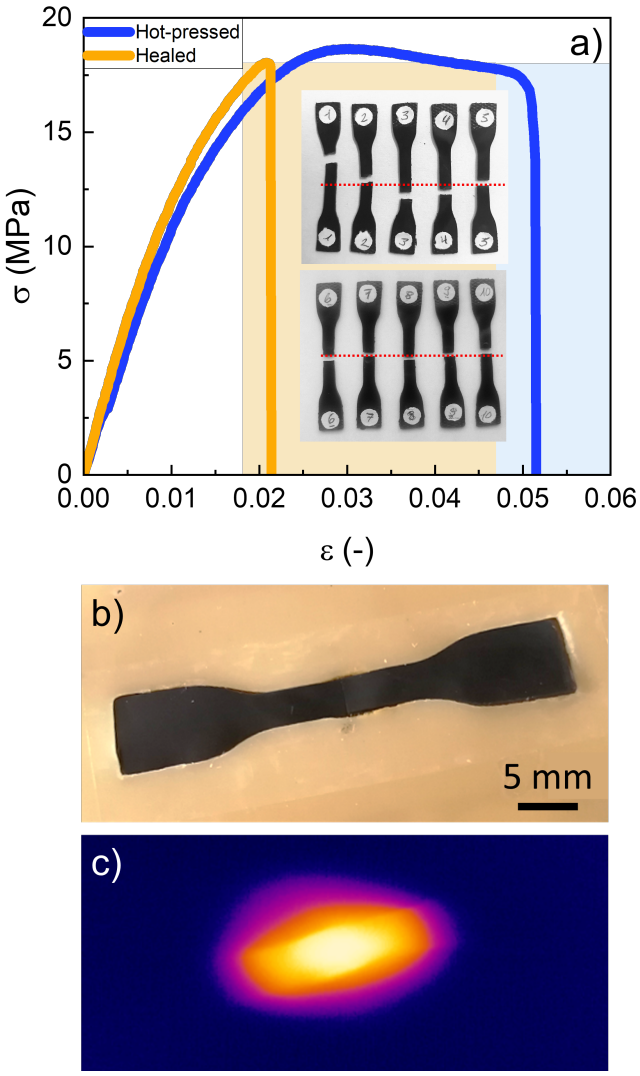

Figure 5: a) Tensile tests of hot-pressed and healed M7 samples. Shaded orange and blue zones indicate the dispersion of the strain at failure. The inset represents a series of hot-pressed (top) and healed (bottom) samples at failure. b-c) M7 dumbbell specimen configuration during cicatrization. Photographs are taken with white and IR light, respectively (see Section II for details).

evidence that the NPs are well distributed within the iPP matrix after hot-pressing and that this structure is preserved in the healed zone. Also, they do not show any particular porosity as one may have expected from the healing of (partly) hydrophilic materials due to sudden moisture evaporation.[17] Besides, cross-section FIB-SEM micrographs taken in the $(\vec{X}, \vec{Z})$ plane at a much higher magnification enabling single NP resolution suggest that the healing procedure involving induction heating may have oriented NPs aggregates according to the magnetic field lines. In fact, while NPs do not present any particular organization in the hot-pressed sample (Figure 6c), the healed version indicate a slight vertical alignment of the aggregates (Figure 6d) that is likely to become evident with increasing the filler content (see *e.g.* refs[17,28]).

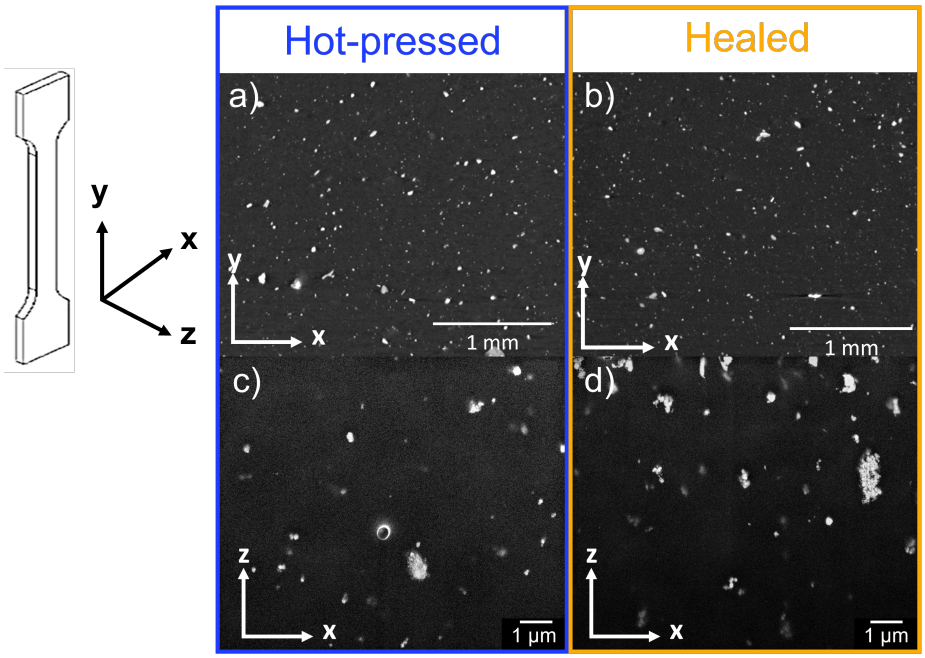

Figure 6: Microstructure of the *hot-pressed* and *healed* M7 samples at various lengthscales. a-b) X-ray tomography slices and c-d) FIB-SEM micrographs. The magnetic field lines during healing are oriented vertically in (d).

Smoothing 3D-parts

Beyond the production of hot-pressed (or equivalently injected) parts, additive manufacturing achieved through Fused Deposition Modeling (FDM) of thermoplastic polymers represents a promising alternative to produce complex architectures likely to modify the design of entire engineering systems in the transport industry. This technology however suffers from a severe compromise between the quality of the printed parts and the time required to produce them, being critically longer than with injection-based methods for large items (> 100 g). Increasing the size of the nozzle and/or the speed of filament deposition to accelerate the manufacturing are notably expected to lead to a larger number of critical defects possibly resulting in catastrophic and premature failure of the operating materials.[48–50] Most common defects include macroscopic anisotropy,[51] residual stress and porosity.[52,53] In this context, magnetic hyperthermia represents an efficient and solvent-free method to smooth the rough surface of 3D-printed parts with the aim to enhance both their mechanical performances and their appearance.

Here, we have 3D-printed kilograms of M7 nanocomposite sheets at a speed relevant for industrial applications from which we have extracted 3.4 mm thick dumbbell specimen. Tensile tests were performed both on these '*as printed*' samples and on their '*smoothed*' counterparts and are presented in Figure 7. The first striking observation is the dramatically lower mechanical properties of the '*as printed*' specimens with respect to their '*hot-pressed*' analogs: i) their Young modulus is close to 700 MPa (*vs.* 1 GPa), ii) the stress at failure is always about 5.5 MPa (*vs.* 18 MPa), where a fragile (*vs.* ductile) rupture is observed, and iii) the strain at failure belongs to the 0.75-1.2% interval (*vs.* 5-7%). The impact of the smoothing procedure seems however quite significant, doubling both the strain and the stress at failure in a systematic way (3 specimens). For the sake of clarity, we have reported the main tensile tests characteristics of all the samples in Table 2.

These results can be rationalized through the scanning electronic microscopy experiments presented in Figure 8, where an '*as printed*' and a partly smoothed sample are investigated.

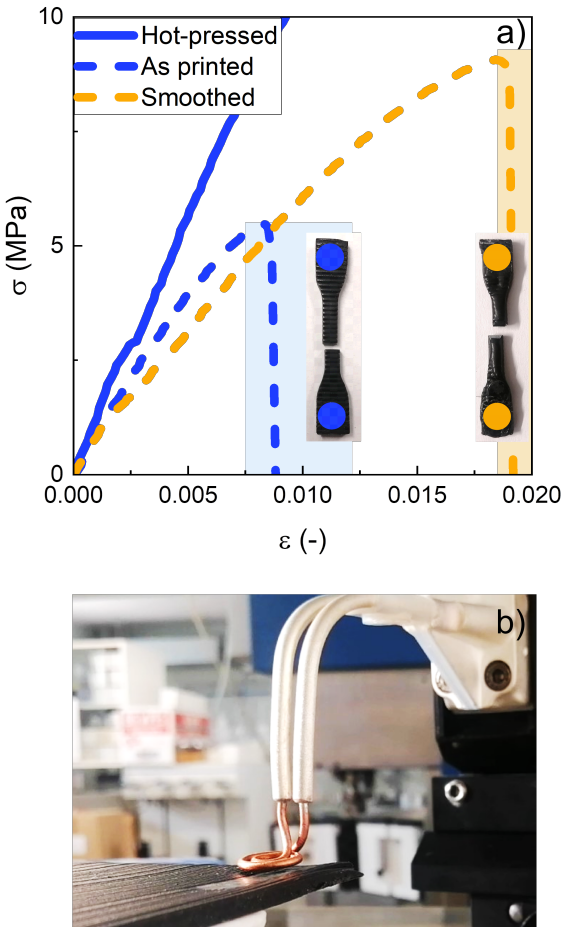

Figure 7: a) Tensile tests of '*as printed*' and '*smoothed*' M7 samples (dashed lines). Analog data for the hot-pressed sample is reported for comparison (solid line). Inset: '*as printed*' and '*smoothed*' specimen at failure. Shaded zones emphasize the dispersion of strain at failure. b) Photograph of the setup configuration used to smooth the 3D-printed samples. The processed zone visibly reflects more light.

Table 2: Representative tensile properties of M7 samples including i) *hot-pressed* and *healed* samples, and ii) *as printed* and *smoothed* ones.

processing	E (MPa)	σ_f (MPa)	ε_f (-)
hot-pressed	1095	18.0	0.051
healed	895	18.0	0.021
as printed (3D)	685 ±21	5.5 ±0.8	0.008 ±0.001
smoothed (3D)	463 ±0.6	8.9 ±0.1	0.019 ±0.00035

Figures 8a-b focuses on the cross section of the '*as printed*' dumbbell specimen, clearly evidencing the presence of a large number of ca. 100 μm pores. This observation confirms therefore that obtaining a homogeneous material from rapid and large scale 3D-printing is far from being trivial and that, apart from the optimization of the printing parameters, a post-treatment is most often required to enhance the quality of the part. From a mechanical point of view, the porosity is expected to reduce the Young modulus and lower both the yield stress and yield strain as observed in Figure 7 (see '*hot-pressed*' *vs.* '*as printed*' samples' performance). It is however interesting to remark that the critical defect size of iPP is expected to be $a_c \approx K_{Ic}^2/(\pi\sigma_f^2) \approx 1$ mm for mode I solicitation,[54] where K_{Ic} is the corresponding plane strain fracture toughness, close to 4 MPa $m^{1/2}$ and σ_f is the yield stress. The value of a_c is thus significantly larger than the pores' size, which should result in a plastic deformation of the '*as printed*' M7 sample before its catastrophic failure. The fact that the opposite trend is observed in Figure 7a suggests therefore that the pores are likely to be connected (forming larger defects) or that their inter-wall distance is smaller than their diameter (modifying the local stress intensity factor). In fact, we remind the reader that the nozzle diameter is 3.5 mm and that in spite of the fused filament compression during the printing, ca. 1 mm roughness remains at the surface of the specimen as evidenced in Figures 8c-d.

Remarkably, the same Figures however emphasize that these large surface heterogeneities are mostly erased when the samples are post-treated with the magnetic field (orange zones). In addition, the internal porosity is not detectable anymore, indicating that the smoothing procedure does act in an efficient way to enhance the quality of the specimen. Figure 8e

focuses on the interface between the healed and native zones of the specimen, revealing a clear difference in terms of fracture pattern. While the (healed) top part exhibits some roughness at large scale ($\approx$ 100 μm), the (native) bottom part is clearly less homogeneous, with a roughness lengthscale closer to 10 μm. These results support the mechanical tests presented in Figure 7a where the dumbbell specimen were treated on both faces, undoubtedly reducing the size of the largest defects present in the material and enhancing therefore its resistance to failure. Nevertheless, the similar Young modulus observed on '*as printed*' and '*smoothed*' samples indicate that apart from the residual geometrical defects, the iPP structure might have been modified by the additive manufacturing. (No significant difference is however observed from DSC thermograms of '*as printed*' and '*hot-pressed*' samples - see **SI Section 3**).

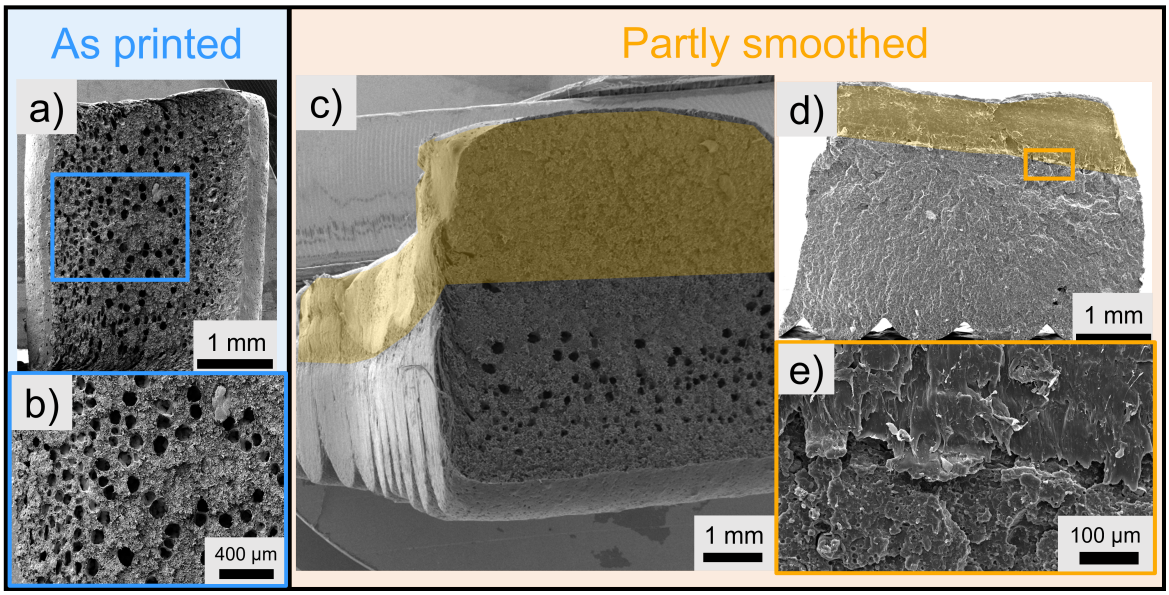

Figure 8: SEM micrographs of 3D-printed samples after tensile failure. a-b) Cross-section of an '*as printed*' sample that exhibits a uniform spatial distribution of milliporosities (blue). c-d-e) Partly smoothed sample highlighting the structural difference between native and smoothed zones (orange).

Conclusion

iPP-based nanocomposites filled with various contents of Fe_3O_4 NPs (x_{NP} = 2-22 wt.%) have been prepared through twin-screw extrusion with the aim to identify a relevant material for the transport industry endowed with the ability to be cicatrized and/or smoothed easily from magnetic hyperthermia. The first step consisted of a systematic characterization of the specific power generated by the NPs under a high frequency oscillatory magnetic field varying both the effective time pulse and the NPs content. As expected, magnetic hysteresis losses were observed to i) scale in a linear way with the former parameter and ii) be independent of the latter. More interestingly, our experiments unambiguously confirmed the presence of a second heating mechanism previously assigned to NPs-polymer friction triggered by the melting of the matrix. The specific power generated by friction was characterized for the first time evidencing its linear evolution with the time pulse while being quasi-independent of the NP content above a certain temperature threshold. Of a particular interest is the fact that the specific power generated through friction was found to be (only) three times lower than the one obtained through magnetic hysteresis losses evidencing that NPs motion is highly relevant to control the temperature of polymeric fluids submitted to magnetic hyperthermia.

From a practical point of view, we produced hot-pressed and 3D-printed specimen for tensile tests based on a nanocomposite containing 7 wt.% of Fe_3O_4 NPs, ensuring both rapid heating up to the iPP melting point and rapid flowing. The ability to heal was evaluated through a rewelding step performed after having cut the specimen into two parts. Tensile experiments evidenced similar stress at failure prior and after the cicatrization whereas the corresponding strain was systematically lower suggesting incomplete inter-diffusion of the polymer at the interface prior to its recrystallization. On the other hand, smoothing 3D-printed specimens (of significantly weaker properties than their hot-pressed counterparts) was found to double both their strain and stress at failure, representing a quite promising result for the development of 3D-printed parts post-processing.

Associated Content

Supplementary Information: 1) Raw materials: XRD pattern of the Fe_3O_4 NPs and SEC of the iPP, 2) Details on the twin screw extruder for large scale production, 3) DSC thermograms of samples with various thermal history and formulations.

Authors information

Corresponding Author : *G.P.B.: guilhem.baeza@insa-lyon.fr

Acknowledgement

All the authors thank Sophie Desmoures (So Sciences) for her help as manager of the "*Smart Polymer Bumper*" project as well as Nathalie Veiga (PO), Philippe Gilotte (PO), Manuel Collet (ECL), Rauf Garip (LINES), Emerik Poursilie (LINES) and Nassim Aliche (LINES) for fruitful discussions and technical support. G.P.B. thanks Lisa-Marie Pouilly, Camille Crouzet and Philippe le Bouteiller (Hymag'in) for their advice on the choice of the magnetite powder. P.G., J.C. and G.P.B. thank the *So Sciences Foundation* for funding allocated to MATEIS within the project *Smart Polymer Bumpers*. This work was supported as part of MANIOC project (Micro-Magnetic Manipulation of Block-Copolymers) funded by the french ANR [ANR-22-CE06-0006-01] as well as the french ministry of research and higher education (L.E. PhD thesis funding).

References

(1) Cordier, P.; Tournilhac, F.; Soulié-Ziakovic, C.; Leibler, L. Self-healing and thermoreversible rubber from supramolecular assembly. *Nature* **2008**, *451*, 977–980.

(2) Rose, S.; Prevoteau, A.; Elzière, P.; Hourdet, D.; Marcellan, A.; Leibler, L. Nanoparticle solutions as adhesives for gels and biological tissues. *Nature* **2014**, *505*, 382–385.

(3) Jourdain, A.; Asbai, R.; Anaya, O.; Chehimi, M. M.; Drockenmuller, E.; Montarnal, D. Rheological properties of covalent adaptable networks with 1, 2, 3-triazolium cross-links: the missing link between vitrimers and dissociative networks. *Macromolecules* **2020**, *53*, 1884–1900.

(4) Van Ruymbeke, E. Preface: Special issue on associating polymers. *Journal of Rheology* **2017**, *61*, 1099–1102.

(5) Zhang, Z.; Chen, Q.; Colby, R. H. Dynamics of associative polymers. *Soft Matter* **2018**, *14*, 2961–2977.

(6) Yang, L.; Tan, X.; Wang, Z.; Zhang, X. Supramolecular polymers: historical development, preparation, characterization, and functions. *Chemical reviews* **2015**, *115*, 7196–7239.

(7) Wang, S.; Urban, M. W. Self-healing polymers. *Nature Reviews Materials* **2020**, *5*, 562–583.

(8) Yang, Y.; Urban, M. W. Self-Healing of Polymers via Supramolecular Chemistry. *Advanced Materials Interfaces* **2018**, *5*, 1800384, _eprint: https://onlinelibrary.wiley.com/doi/pdf/10.1002/admi.201800384.

(9) Hayashi, M.; Tournilhac, F. Thermal stability enhancement of hydrogen bonded semicrystalline thermoplastics achieved by combination of aramide chemistry and supramolecular chemistry. *Polymer Chemistry* **2017**, *8*, 461–471.

(10) Louhichi, A.; Jacob, A.; Bouteiller, L.; Vlassopoulos, D. Humidity affects the viscoelastic properties of supramolecular living polymers. *Journal of Rheology* **2017**, *61*, 1173–1182.

(11) Simonin, L.; Falco, G.; Pensec, S.; Dalmas, F.; Chenal, J.-M.; Ganachaud, F.; Marcellan, A.; Chazeau, L.; Bouteiller, L. Macromolecular additives to turn a thermoplastic elastomer into a self-healing material. *Macromolecules* **2021**, *54*, 888–895.

(12) Zhang, L.; Zhang, Z.; Yu, W.; Miao, Y. Review of the Application of Microwave Heating Technology in Asphalt Pavement Self-Healing and De-icing. *Polymers* **2023**, *15*, 1696.

(13) Solouki Bonab, V.; Karimkhani, V.; Manas-Zloczower, I. Ultra-Fast Microwave Assisted Self-Healing of Covalent Adaptive Polyurethane Networks with Carbon Nanotubes. *Macromolecular Materials and Engineering* **2019**, *304*, 1800405.

(14) Launay, V.; Caron, A.; Noirbent, G.; Gigmes, D.; Dumur, F.; Lalevée, J. NIR organic dyes as innovative tools for reprocessing/recycling of plastics: Benefits of the photothermal activation in the near-infrared range. *Advanced Functional Materials* **2021**, *31*, 2006324.

(15) Li, X.; Wang, H.; Yuan, S.; Lin, S.; Deng, S.; Du, Z.; Cheng, X.; Du, X. NIR-induced self-healing and recyclable polyurethane composites based on thermally reversible crosslinking for efficient solar-to-thermal energy storage. *Polymer* **2022**, *250*, 124885.

(16) Yang, Y.; He, J.; Li, Q.; Gao, L.; Hu, J.; Zeng, R.; Qin, J.; Wang, S. X.; Wang, Q. Self-healing of electrical damage in polymers using superparamagnetic nanoparticles. *Nature nanotechnology* **2019**, *14*, 151–155.

(17) Griffiths, P.; Coativy, G.; Dalmas, F.; Falco, G.; Jiang, L.; Xiang, Z.; Le, M.-Q.; Ducharne, B.; Le Roy, D.; Méchin, F.; others Ultrafast Remote Healing of Magneto-Responsive Thermoplastic Elastomer-Based Nanocomposites. *Macromolecules* **2022**, *55*, 831–843.

(18) Corten, C. C.; Urban, M. W. Repairing polymers using oscillating magnetic field. *Advanced materials* **2009**, *21*, 5011–5015.

(19) Hohlbein, N.; Shaaban, A.; Schmidt, A. Remote-controlled activation of self-healing behavior in magneto-responsive ionomeric composites. *Polymer* **2015**, *69*, 301–309.

(20) Ahmed, A. S.; Ramanujan, R. V. Magnetic field triggered multicycle damage sensing and self healing. *Scientific reports* **2015**, *5*, 13773.

(21) Mehdaoui, B.; Meffre, A.; Carrey, J.; Lachaize, S.; Lacroix, L.-M.; Gougeon, M.; Chaudret, B.; Respaud, M. Optimal size of nanoparticles for magnetic hyperthermia: a combined theoretical and experimental study. *Advanced Functional Materials* **2011**, *21*, 4573–4581.

(22) Deatsch, A. E.; Evans, B. A. Heating efficiency in magnetic nanoparticle hyperthermia. *Journal of Magnetism and magnetic Materials* **2014**, *354*, 163–172.

(23) Carrey, J.; Mehdaoui, B.; Respaud, M. Simple models for dynamic hysteresis loop calculations of magnetic single-domain nanoparticles: Application to magnetic hyperthermia optimization. *Journal of applied physics* **2011**, *109*.

(24) Coey, J. M. *Magnetism and magnetic materials*; Cambridge university press, 2010.

(25) Hiergeist, R.; Andrä, W.; Buske, N.; Hergt, R.; Hilger, I.; Richter, U.; Kaiser, W. Application of magnetite ferrofluids for hyperthermia. *Journal of magnetism and Magnetic Materials* **1999**, *201*, 420–422.

(26) Bayerl, T.; Schledjewski, R.; Mitschang, P. Induction heating of thermoplastic materials by particulate heating promoters. *Polymers and Polymer Composites* **2012**, *20*, 333–342.

(27) Jiang, L.; Griffiths, P.; Balouet, J.; Faure, T.; Lyons, R.; Fustin, C.-A.; Baeza, G. P.

Magneto-Responsive Nanocomposites with a Metal–Ligand Supramolecular Matrix. *Macromolecules* **2022**, *55*, 3936–3947.

(28) Pommella, A.; Griffiths, P.; Coativy, G.; Dalmas, F.; Ranoo, S.; Schmidt, A. M.; Méchin, F.; Bernard, J.; Zinn, T.; Narayanan, T.; others Fate of Magnetic Nanoparticles during Stimulated Healing of Thermoplastic Elastomers. *ACS nano* **2023**, *17*, 17394–17404.

(29) Landi, G. T. Simple models for the heating curve in magnetic hyperthermia experiments. *Journal of magnetism and magnetic materials* **2013**, *326*, 14–21.

(30) Helbig, S.; Abert, C.; Sánchez, P. A.; Kantorovich, S. S.; Suess, D. Self-consistent solution of magnetic and friction energy losses of a magnetic nanoparticle. *Physical Review B* **2023**, *107*, 054416.

(31) Pousthomis, M.; Anagnostopoulou, E.; Panagiotopoulos, I.; Boubekri, R.; Fang, W.; Ott, F.; Atmane, K. A.; Piquemal, J.-Y.; Lacroix, L.-M.; Viau, G. Localized magnetization reversal processes in cobalt nanorods with different aspect ratios. *Nano Research* **2015**, *8*, 2231–2241.

(32) Anagnostopoulou, E.; Grindi, B.; Lacroix, L.-M.; Ott, F.; Panagiotopoulos, I.; Viau, G. Dense arrays of cobalt nanorods as rare-earth free permanent magnets. *Nanoscale* **2016**, *8*, 4020–4029.

(33) Wang, C.; Hsu, C.-H.; Li, Z.; Hwang, L.-P.; Lin, Y.-C.; Chou, P.-T.; Lin, Y.-Y. Effective heating of magnetic nanoparticle aggregates for in vivo nano-theranostic hyperthermia. *International Journal of Nanomedicine* **2017**, 6273–6287.

(34) Palanikumar, K.; AshokGandhi, R.; Raghunath, B.; Jayaseelan, V. Role of Calcium Carbonate (CaCO3) in improving wear resistance of Polypropylene (PP) components used in automobiles. *Materials Today: Proceedings* **2019**, *16*, 1363–1371.

(35) Gallone, T.; Zeni-Guido, A. Closed-loop polypropylene, an opportunity for the automotive sector. *Field Actions Science Reports. The journal of field actions* **2019**, 48–53.

(36) Brunet, F.; Crouzet, C.; Goffe, B. Method for producing nanomagnetite. 2020; US Patent 10,843,935.

(37) Crouzet, C.; Brunet, F.; Recham, N.; Auzende, A.-L.; Findling, N.; Magnin, V.; Ferrasse, J.-H.; Goffé, B. Hydrothermal steel slag valorization—Part II: Hydrogen and nano-magnetite production. *Frontiers in Earth Science* **2017**, *5*, 86.

(38) Nagoshi, M.; Kawano, T.; Sato, K. Simple separations of topographic and material contrasts using one annular type in-lens detector of low-voltage SEM. *Surface and Interface Analysis* **2016**, *48*, 470–473.

(39) Griffiths Alfaro, P. Magnetic induction healing of thermoplastic elastomer composites : Multi-physics characterization - Appendix B. Ph.D. thesis, 2022.

(40) Li, J.; Cheung, W.; Jia, D. A study on the heat of fusion of β-polypropylene. *Polymer* **1999**, *40*, 1219–1222.

(41) Sirota, E.; King Jr, H.; Singer, D.; Shao, H. H. Rotator phases of the normal alkanes: An x-ray scattering study. *The Journal of chemical physics* **1993**, *98*, 5809–5824.

(42) Di Giambattista, C.; Sanctuary, R.; Perigo, E.; Baller, J. Relaxations in the metastable rotator phase of n-eicosane. *The Journal of chemical physics* **2015**, *143*.

(43) Denkov, N.; Tcholakova, S.; Lesov, I.; Cholakova, D.; Smoukov, S. K. Self-shaping of oil droplets via the formation of intermediate rotator phases upon cooling. *Nature* **2015**, *528*, 392–395.

(44) Androsch, R.; Di Lorenzo, M. L.; Schick, C.; Wunderlich, B. Mesophases in polyethylene, polypropylene, and poly (1-butene). *Polymer* **2010**, *51*, 4639–4662.

(45) Guerra, G.; Petraccone, V.; Corradini, P.; De Rosa, C.; Napolitano, R.; Pirozzi, B.; Giunchi, G. Crystalline order and melting behavior of isotactic polypropylene (α form). *Journal of Polymer Science: Polymer Physics Edition* **1984**, *22*, 1029–1039.

(46) Mark, J. E.; others *Physical properties of polymers handbook*; Springer, 2007; Vol. 1076.

(47) Chase, M. W. NIST-JANAF Themochemical Tables, Fourth Edition. **1998**, 1–1951.

(48) Riddick, J. C.; Haile, M. A.; Wahlde, R. V.; Cole, D. P.; Bamiduro, O.; Johnson, T. E. Fractographic analysis of tensile failure of acrylonitrile-butadiene-styrene fabricated by fused deposition modeling. *Additive Manufacturing* **2016**, *11*, 49–59.

(49) Lay, M.; Thajudin, N. L. N.; Hamid, Z. A. A.; Rusli, A.; Abdullah, M. K.; Shuib, R. K. Comparison of physical and mechanical properties of PLA, ABS and nylon 6 fabricated using fused deposition modeling and injection molding. *Composites Part B: Engineering* **2019**, *176*, 107341.

(50) Singh, S.; Singh, G.; Prakash, C.; Ramakrishna, S. Current status and future directions of fused filament fabrication. *Journal of Manufacturing Processes* **2020**, *55*, 288–306.

(51) Ahn, S.; Montero, M.; Odell, D.; Roundy, S.; Wright, P. K. Anisotropic material properties of fused deposition modeling ABS. *Rapid Prototyping Journal* **2002**, *8*, 248–257, Publisher: MCB UP Ltd.

(52) Samy, A. A.; Golbang, A.; Harkin-Jones, E.; Archer, E.; Tormey, D.; McIlhagger, A. Finite element analysis of residual stress and warpage in a 3D printed semi-crystalline polymer: Effect of ambient temperature and nozzle speed. *Journal of Manufacturing Processes* **2021**, *70*, 389–399.

(53) Zhang, W.; Wu, A. S.; Sun, J.; Quan, Z.; Gu, B.; Sun, B.; Cotton, C.; Heider, D.; Chou, T.-W. Characterization of residual stress and deformation in additively manu-

factured ABS polymer and composite specimens. *Composites Science and Technology* **2017**, *150*, 102–110.

(54) Ashby, M. F.; Johnson, K. *Materials and design: the art and science of material selection in product design*; Butterworth-Heinemann, 2013.

TOC Graphic